Dalton Transactions

Accepted Manuscript

This is an *Accepted Manuscript*, which has been through the Royal Society of Chemistry peer review process and has been accepted for publication.

Accepted Manuscripts are published online shortly after acceptance, before technical editing, formatting and proof reading. Using this free service, authors can make their results available to the community, in citable form, before we publish the edited article. We will replace this *Accepted Manuscript* with the edited and formatted *Advance Article* as soon as it is available.

You can find more information about *Accepted Manuscripts* in the Information for Authors.

Please note that technical editing may introduce minor changes to the text and/or graphics, which may alter content. The journal's standard Terms & Conditions and the Ethical guidelines still apply. In no event shall the Royal Society of Chemistry be held responsible for any errors or omissions in this *Accepted Manuscript* or any consequences arising from the use of any information it contains.

ROYAL SOCIETY OF CHEMISTRY

www.rsc.org/dalton

Please do not adjust margins

Journal Name

ARTICLE

Synthesis, Structure and Properties of the Manganese-doped Polyoxotitanate Cage $[Ti_{18}MnO_{30}(OEt)_{20}(MnPhen)_3]$ (Phen = 1,10-Phenanthroline)

Received 00th January 20xx,
Accepted 00th January 20xx

DOI: 10.1039/x0xx00000x

www.rsc.org/

Ning Li,[ab] Peter D. Matthews,[a] Jane J. Leung,[a] Timothy C. King,[a] Paul T. Wood,[a] He-Kuan Luo,[b] and Dominic S. Wright*[a]

The novel heterometallic polyoxotitanate cage $[Ti_{18}MnO_{30}(OEt)_{20}(MnPhen)_3]$ (**1**), obtained by solvothermal reaction of $Ti(OEt)_4$ with $Mn(AcO)_3{\cdot}(H_2O)_2$ and 1,10-phenanthroline (Phen) in EtOH, has a C_3 symmetric core structure containing an interstitial tetrahedral Mn^{II} ion and is surrounded by three Mn^{II}(Phen) fragments. The molecular structure is retained in thin film electrodes of **1** deposited by solution drop-casting onto fluorinated tin oxide (FTO). Both solid state and solution phase electrochemical measurements show dual redox couples, consistent with the two distict Mn coordination environments in the cage structure. Sintering of **1** in air at 600 °C produces a black crystalline solid which consists of Mn-doped TiO_2 (mainly in the rutile phase) together with α-Mn_2O_3. Such a composite semiconductor has an optical band gap of *ca.* 1.80 eV, similar to that of α-Mn_2O_3.

Introduction

In recent years, titania (TiO_2) has attracted a great deal of attention as a highly stable and environmentally benign semiconductor,[1] and it has important applications in state-of-the-art photochromic, photocatalytic and photovoltaic devices.[2,3] However, the large band gap of TiO_2 (*ca.* 3.2 eV), which is at the edge of the visible region, severely limits its photonic application using ambient sunlight. An important method of reducing the band gap is the incorporation of metal dopant ions into the structure of TiO_2, which introduces accessible band gap states for electronic transitions and this area is a major focus of current research worldwide.

Resembling the fragments of bulk TiO_2, molecular polyoxotitanate (POT) cages of the type $[Ti_xO_y(OR)_z]$ and metal-doped cages (M-POT) $[Ti_xO_y(OR)_z(M)_n]$ have well-defined inorganic Ti_xO_y cores and can be seen as models for the study of structural chemistry of bulk TiO_2, such as its crystal growth,[4,5] the binding of surface sensitizers,[6-14] and the electronic and structural effects of heterometallic doping.[15-27] These cages also possess hydrolysable organic alkoxy ligand peripheries and can function as single-source precursors for the solution deposition of TiO_2 and metal-doped TiO_2.[28-30]

The current research trends in the POT and M-POT field have mainly focused on three aspects. The first is to increase the Ti_xO_y core size in order to obtain atomically defined homo-dispersed nanoparticles with unique dimensions and structures. So far the largest undoped single-core POT cage contains 28 titanium atoms in total.[15] More commonly, POT cages containing Ti_4, Ti_7 and Ti_{16} cores are formed, often as side-products in solvothermal POT synthesis. Inspired by the extensive investigation of metal-doped TiO_2 materials,[31,32] a second strand of research has been to introduce heterometallic ions into the POT structure. To date, various metals have been incorporated into such M-POTs, including *d*-block metals,[16-25] lanthanides[26,27] and alkali metals.[15,17] The influences of these heterometallic ions on optical, electrochemical and photocatalytic properties have also been under systematic studies by our group and others.[16-19,21,23,27] Drawing on the concept of the bonding of dye-sensitized surface molecules on TiO_2, a third aspect of research concerns cages containing 'surface-bonded' functional molecules. Catechol-modified POTs were firstly reported almost a decade ago and such clusters are red in colour due to the charge transfer from catechol to the Ti_xO_y cores of POTs.[14,33,34] The use of ligands like 9-anthracenecarboxylate and 1,10-phenanthroline in the cages (i.e. $[Ti_6O_6(O^iPr)_6(9\text{-AC})_6]$, $[Ti_6O_4(O^iPr)_6(cat)_4(9\text{-AC})_2]$ and $[Ti_{17}O_{28}(O^iPr)_{16}(M^{II}phen)_2]$ (M = Co, Cd, Fe)) has been reported recently, which facilitates fluorescence and/or photocurrent generation.[6,8,10]

In the present study, we report the synthesis, structure and properties of the new M-POT cage $[Ti_{18}MnO_{30}(OEt)_{20}(MnPhen)_3]$ (**1**), having a C_3-symmetric $Ti_{18}Mn_4O_{30}$ core arrangement with the Mn dopants in two distinct environments. The optical and electrochemical properties of **1** are explored, along with the formation of black,

[a] *Department of Chemistry, University of Cambridge, Lensfield Road, Cambridge, CB2 1EW, UK. *E-mail: dsw1000@cam.ac.uk*
[b] *Institute of Materials Research and Engineering, Agency for Science Technology and Research (A*STAR), 2 Fusionopolis Way, #08-03, Innovis, Singapore 138634.*
Electronic Supplementary Information (ESI) available: IR of **1**, XPS of **1**, IR and SEM of electrochemical films and sintered samples. See DOI: 10.1039/x0xx00000x

This journal is © The Royal Society of Chemistry 20xx

Dalton Transactions Accepted Manuscript

Please do not adjust margins

'Mn-doped' TiO_2 directly from **1** (consisting of α-Mn_2O_3 and TiO_2).

Results and Discussion

The new cage $[Ti_{18}MnO_{30}(OEt)_{20}(MnPhen)_3]$ (**1**) was obtained by the solvothermal reaction of $Ti(OEt)_4$ with $Mn(AcO)_3{\cdot}(H_2O)_2$ and 1,10-phenanthroline (19 : 1 : 1 equivalents) in anhydrous EtOH at 150 °C for 72 h (Scheme 1). Slow cooling of the reaction to room temperature gave orange block-shaped crystals of **1** in 20% yield.‡ The reaction conditions and stoichiometry involved are similar to those used previously in the synthesis of the related Mn^{II}-based cages $[Ti_{27}MnKO_{35}(OH)_2(OEt)_{39}]_{0.33}[Ti_{28}MnKO_{37}(OH)(OEt)_{40}]_{0.67}$ (**2**) and $[Ti_{14}O_{14}(OH)_2(OEt)_{28}Mn]$ (**3**), in the absence of 1,10-phenanthroline.[17,20]

Scheme 1. Synthetic conditions used to obtain the new cage **1**.

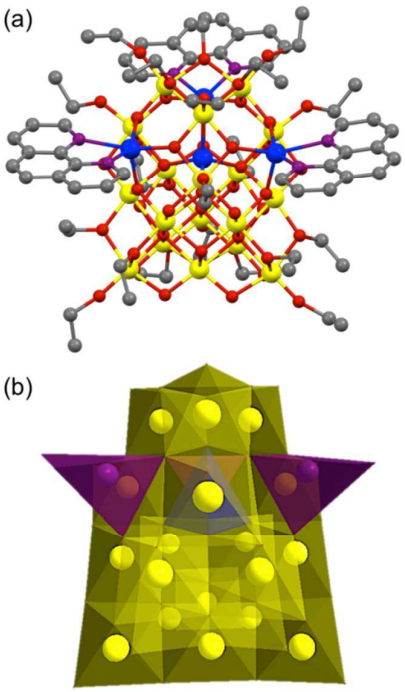

Figure 1. (a) The structure of the cage molecule **1**, showing a view from the side. H-atoms are omitted for clarity. Selected bond lengths (Å) and angles (°): Mn(interstitial)-O 2.053(8)-2.070(10), Mn(peripheral)-O 2.080(10)-2.120(10), Mn(peripheral)-N 2.250(10)-2.280(10), Ti-O 1.730(10)-2.340(10), O-Mn(interstitial)-O 106.0(4)-113.5(4), O-Mn(peripheral)-O 98.7(4)-100.6(4), N-Mn(peripheral)-N 70.5(3)-72.3(3), O-Ti-O_{trans} 74.3(4)-106.7(5), O-Ti-O_{cis} 151.2(5)-178.7(4). (yellow = Ti, blue = Mn, purple = N, red = O, grey = C). (b) The polyhedral representation of the cage core containing 18 octahedral Ti (yellow), 3 trigonal bipyramidal Mn (purple) and 1 tetrahedral Mn (blue).

Owing to the paramagnetic character of **1** arising from the presence of four high-spin d^5 Mn^{II} ions, NMR spectroscopy was of no value in its characterisation. Although the IR spectrum of **1** confirmed the presence of the 1,10-phenantholine ligands (Figure S1, ESI), single-crystal X-ray diffraction was the primary tool used in the initial characterisation of **1**.§ Cage molecules of **1** consist of a C_3-symmetric $Ti_{18}Mn_4O_{30}$ polyoxotitanate in which all of the Ti^{IV} atoms are six-coordinate (Figure 1). The core of the cage shares some similarities with the major polymorphs of TiO_2 (rutile, anatase and brookite), such as the exclusively six-fold coordination of all Ti atoms and μ_3-O bridges.[14] One of the four Mn^{II} centres in **1** is located in an interstitial, tetrahedral coordination site (being bonded to four oxo-atoms of the core). The remaining three, symmetry-related Mn^{II} ions are complexed at the periphery of the cage and have approximate trigonal bipyramidal geometries, being bonded to three μ_3-O atoms of the core and the two N atoms of the 1,10-phenanthroline ligand. To the best of our knowledge, cage **1** is the first M-POT structure with a single type of metal dopant (Mn^{II}) in two distinct coordination environments. The indication of exclusively Mn^{II} within **1** comes from X-ray photoelectron spectroscopy (XPS) on the cage, in which the observed splitting of the doublet Mn 3s peaks (*ca.* 6.0 eV) is in line with the literature values for Mn^{II} (Figure S2, ESI).[35,36]

Direct support for the crystallographic formulation of **1** comes from the high-resolution +ve ion ESI mass spectrum. The higher mass region of the spectrum is shown in Figure 2c, with the simulated isotopic pattern for the molecular ion being compared with the experimental envelope in Figures 2a and 2b, respectively. The experimental isotope pattern agrees well with the simulated data for the molecular ion, calculated from the crystal structure ($[M]^+$ m/z = 3004.5588, cald. 3004.5575). Some of the peaks found above the molecular ion also appear, probably originating from the molecular ion picking up extraneous solvent molecules, i.e., the $[M + toluene]^+$ (found 3096.6517, cald. 3096.6201) and $[M + 2MeOH]^+$ (found 3068.5906, cald. 3068.6099).

One striking feature of crystalline and powdered samples of **1** is their stability in air, even in contact with water under moderately acidic conditions (≥ pH ~ 3). As can be seen from Figure 3, which compares the powder XRD pattern of a crystalline sample of **1** ground in air with the theoretical pattern, the bulk material contains few if any impurities. This conclusion is also supported by elemental analysis, in which the experimentally-measured weight percentages of C, H and N all match well with the calculated values from the solid state structure (see experimental). Crystals of **1** remain intact for several days in ambient air without any visible degradation and there is no change in the powder XRD pattern after *ca.* 30 h exposure to air. It is common to obtain mixtures of cage products in solvothermal synthesis of M-POT cages and for these cages to be moderately or even extremely moisture-sensitive, degrading into low band gap metal-doped TiO_2. The isolation of a single cage component and the prolonged stability of **1** in air are therefore important in respect to the

Dalton Transactions Accepted Manuscript

This journal is © The Royal Society of Chemistry 20xx

Please do not adjust margins

meaning of the analysis of its optical and electrochemical properties which are explored later in this paper.

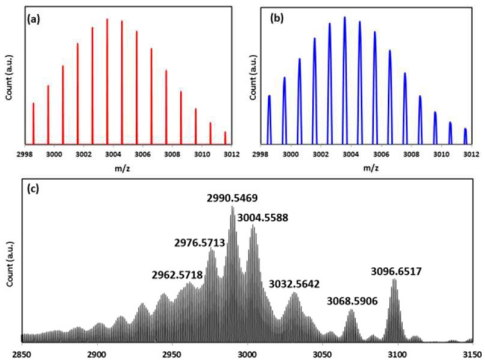

Figure 2. Mass spectrometry of compound **1**: (a) simulated and (b) experimental isotope distribution pattern for the molecular ion. (c) The full MS spectrum, in which some representative data are shown. The sample used was prepared by dissolving a few crystal blocks of **1** in a mixture of toluene and methanol (3:2 volume ratio).

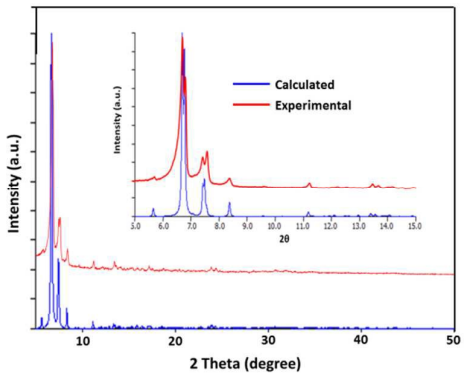

Figure 3. Comparison of the calculated (blue) and experimental (red) powder XRD spectra of compound **1**; the inset is the magnification of the region from 5° to 15°, in which most peaks are located.

The optical properties of **1** were explored using UV-visible reflectance measurements. Although previous analysis had shown that **1** is air- and moisture-stable for prolonged periods at room temperature, high-purity crystalline samples of the cage were ground into powders in a glove box and sealed between quartz windows before transferring to the spectrometer. This was done in order to ensure that there was no possibility of surface aerial hydrolysis of the sample, which would give Mn-doped TiO_2 with a low band gap of *ca.* 2.7 eV.[17] Figure 4a presents the raw UV-visible reflectance data in the form of a plot of the Kubelka-Munk function F(R) *vs.* the incident photon energy, while Figure 4b shows a plot of $[F(R)h\nu]^2$ and assumes a direct band gap semiconductor model (in red in both figures). The blue plots in both figures are the corresponding UV-Vis data for 1,10-phenanthroline itself, illustrating that the band gap cut-offs do not result from this ligand alone. Both of these graphs provide the means of estimating the band gap (or HOMO-LUMO excitation), by extrapolation to zero on the *x*-axis of the linear section of the plots at the cut-off (the dotted lines in each plot). In the case of the raw data (Figure 4a), a band gap of *ca.* 2.95 eV is determined, while the $[F(R)h\nu]^2$ data (Figure 4b) gives a band gap of *ca.* 3.15 eV. These values are consistent with our previous work, which showed that the band gaps determined by the direct extrapolation of the data are normally lower than those determined assuming a direct band gap by around 0.2 eV.[17] Previous studies have suggested that the band gaps for M-POT cages in the solid state are higher than those found for bulk metal-doped TiO_2 but overlap with metal-doped TiO_2 nano-particles.[28] The value found for **1** (2.95-3.15 eV) is in the expected range.

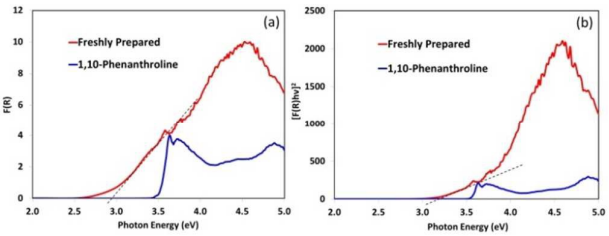

Figure 4. UV-visible reflectance data for **1**, (a) directly measured Kubelka-Munk function F(R), and (b) modified Kubelka-Munk function $[F(R)h\nu]^2$ assuming a direct allowed transition.

Electrochemical analysis was carried out using a drop-cast electrode of **1** on an FTO substrate (denoted as FTO|**1**).[§§] The cage retains its molecular structure after drop-casting, as shown by the IR spectrum of FTO|**1** which is almost identical to that of solid **1** (Figure S3, ESI). Moreover, **1** also appears to survive further electrochemical measurements in aqueous solution (Figure S3, ESI). Cyclic voltammetry (CV) on FTO|**1** at a scan rate of 50 mV/s is shown in Figure 5a. It exhibits oxidation and reduction waves at 1.44 V and 1.22 V *vs.* RHE, respectively, which we attributed to the Mn^{II}/Mn^{III} couple. Confirming this, a similar redox wave is also observed for an FTO electrode coated with the Mn^{II}-based cage $[Ti_{27}MnKO_{35}(OH)_2(OEt)_{39}]_{0.33}[Ti_{28}MnKO_{37}(OH)(OEt)_{40}]_{0.67}$ (**2**) (FTO|**2**).[17] While there is no such wave for FTO coated with the undoped POT cage $[Ti_7O_4(OEt)_{20}]$ (FTO|Ti_7)[37] or for a bare FTO electrode (Figure 5a). In addition, following the Mn^{II}/Mn^{III} oxidation, a further large anodic response emerges and exhibits an onset potential of 1.73 V, while the unmodified FTO, FTO|Ti_7 and FTO|**2** electrodes all show more positive onset potentials of *ca.* 1.88 V. Such a cathodic shift for **1** is unlikely to result from water oxidation catalysis because the electrode stability test shows exponential decay of the current density with time (Figure S4, ESI). The detailed mechanism is subject to further investigation. Furthermore, a second minor redox wave becomes more apparent with the increase of CV scan rate, which resides next to the major wave (at 1.44 V) as discussed above (Figure S5a, ESI).

The presence of the second minor redox wave is also confirmed by solution phase electrochemical analysis using glassy carbon as working electrode (Figure 5b).[§§§] The

Dalton Transactions Accepted Manuscript

Please do not adjust margins

observation of two Mn^{II}/Mn^{III} redox couples for **1** is consistent with the presence of two Mn^{II} coordination environments in the cage. In the solution phase CV scans, the magnitude of each oxidation peak is found to be linearly proportional to the square root of the applied scan rate (inset of Figure S5b, ESI), from which the value of $n^{1.5}D^{0.5}$ can be calculated for both Mn environments using the Randles-Sevcik equation (n being the number of electrons transferred and D the diffusion coefficient). However, it is not possible to say which Mn^{II} environment in the structure of the cage (interstitial or peripheral) corresponds to each wave from the electrode or solution data at this stage.

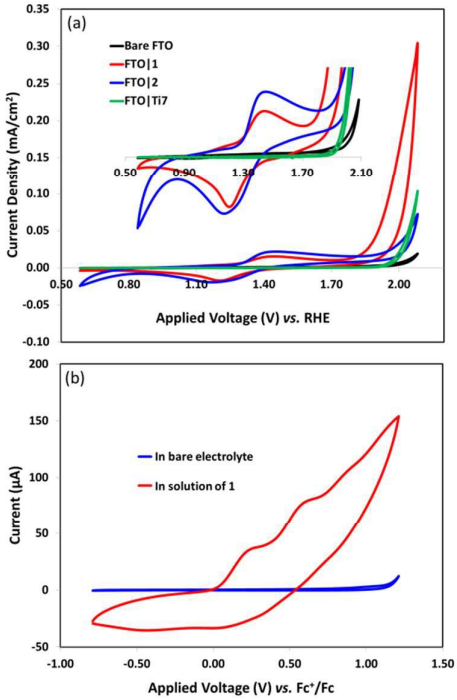

Figure 5. (a) CV of the FTO|**1** (red), FTO (black), FTO|Ti_7 cage (green) and FTO|**2** (blue) electrodes; the scan rate is 50 mV/s and the electrolyte is 0.1 M Na_2SO_4 with pH 6.54. Inset is the magnification of the redox waves. (b) Solution phase CV of **1** using a saturated solution in toluene and methanol mixture; the scan rate is 100 mV/s and the electrolyte is 0.1 M NBu_4BF_4.

The freshly prepared FTO|**1** electrode exhibits a uniform distribution of **1**, as observed by scanning electron microscopy (SEM) (Figure 6a). The magnified image (Figure 6b) shows that the electrode surface is covered by self-assembled spheres (or microcrystals) of **1** of various sizes, spanning from 300 nm – 2.10 μm in diameter. After the electrochemical test, the active film on the FTO remains intact by the naked eye; however, SEM shows aggregation of the spheres into clusters and less uniform distribution of the material compared to the pre-test morphology (Figure 6c and d). No significant change in the size distribution of the spheres was observed between the pre- and post-test electrodes.

Another electrode prepared by drop-casting the same solution of **1** at room temperature was made in order to help to reveal the mechanism of formation of the spherical microcrystals. The film formed is inhomogeneous by the naked eye. Although SEM shows that spherical microcrystals are still produced, they only cover a limited portion of the FTO substrate (Figure 6e). Magnification (Figure 6f) shows that the spheres are much larger compared with those drop-cast at 80 °C (range 700 nm – 4.25μm). Some interesting doughnut-like structures are also observed, which provide some indication of the mechanism of sphere growth. At room temperature, the solvent evaporation rate is much slower than that at higher temperature. Therefore, there is a slower rate of crystal growth, leading to larger spheres. However, presumably if the spheres become too large they can no longer hold their spherical shape. The structures start to collapse and form the doughnut-like objects observed. Dai and colleagues have reported such self-assembled spherical and/or doughnut-like morphologies by drop-casting a solution of the complex $[Ti_{17}O_{28}(O^iPr)_{16}(Co^{II}phen)_2]$ onto ITO.[6]

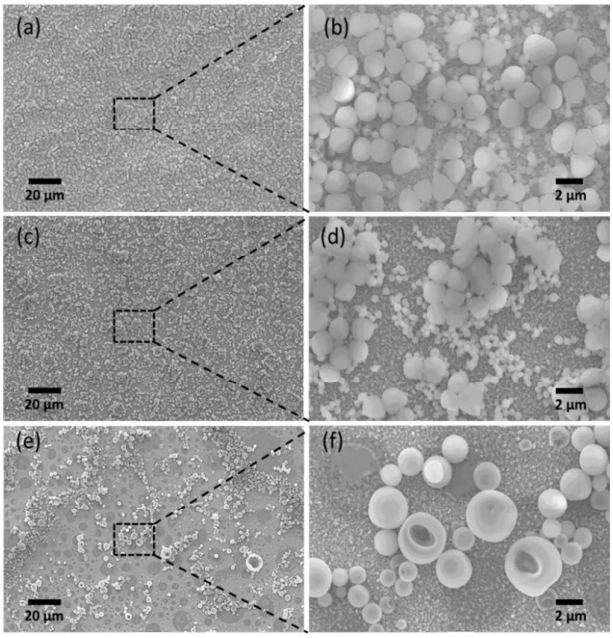

Figure 6. SEM images of the prepared electrode: (a) & (b) FTO|**1** before the electrochemical test, (c) & (d) FTO|**1** after electrochemical test, (e) & (f) FTO|**1** drop-cast at room temperature.

The thermal stability of **1** was investigated using TGA, in the presence of a N_2 flow, coupled with mass spectrometry for exit gas analysis. As shown in Figure 7, weight loss from compound **1** takes place in several stages. The first stage occurs below 100 °C, corresponding to a *ca.* 1.5 wt. % loss. This is assumed to be the result of the release of absorbed moisture from the sample surface, shown by the observation of water in the mass spectrum (inset of Figure 7). The second stage (*ca.* 4.9 wt. %) occurs in the range 100–305 °C, possibly arising from the partial pyrolysis of the ethyl and phenanthroline ligands, as the mass spectrometric signals of H_2O and CO_2 both increase. This is also supported by the

Dalton Transactions Accepted Manuscript

This journal is © The Royal Society of Chemistry 20xx

observation of similar thermal decomposition in the same temperature ranges for commercial 1,10-phenanthroline powder as well as $[Ti_7O_4(OEt)_{20}]$ (data not shown). In the next stage from 305–350 °C, there is a net loss of 13.9 wt. %. We, again, attributed this to the decomposition of the organic ligands of **1**, as sharp signals are observed in the mass spectrum for H_2O and CO_2 ions at the transition temperature of 345 °C. In the higher temperature range up to 800 °C, the weight continues to decrease slowly. This could be due to some further decomposition of the remaining organic groups in **1**, as suggested by elemental analysis on the solid residue before and after heating in the range 600–800 °C, revealing a further reduction in the C, H and N content. The formation of manganese oxides MnO_x at this stage is indicated by the black appearance of the final sample.

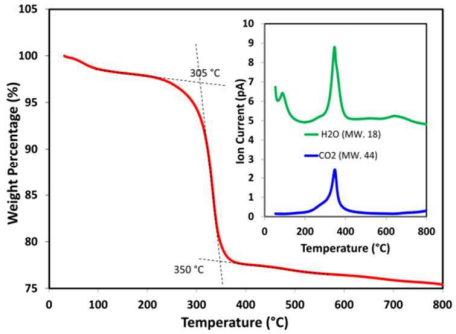

Figure 7. TGA of compound **1** in N_2 flow (100 mL/min) with temperature ramping rate of 5 °C/min. Inset is the monitoring of the ion concentration of H_2O and CO_2 from the exit gases using the mass spectrometric accessory.

Similar to other Mn-POTs, sintering the ground powders of **1** at 500 °C or above in air produces Mn-doped TiO_2. The ground powder of **1** remains crystalline until 200 °C, and crystallizes into TiO_2 at 500 °C (Figure 8). The resulting XRD peaks can be unambiguously assigned to rutile (JCPDS 21-1276) and anatase (JCPDS 89-4921) TiO_2. The major polymorph is rutile, with the (101), (111) and (211) peaks at 36.09°, 41.23° and 54.32° being shifted towards higher angles by 0.11–0.23°, probably owning to the substitution of Ti with Mn atoms in the TiO_2 lattice. Generally, a temperature of 500 °C is not high enough to form the rutile phase of TiO_2. The emergence of rutile in the present case is probably due to the effect of Mn ion doping which is known to be able to promote the stability of the rutile phase.[38,39] Further sintering **1** at 600 °C for 12 h leads to nearly 100% conversion to rutile TiO_2, except for some extraneous peaks that could be well assigned to α-Mn_2O_3.[39] The data therefore suggests that the black material generated eventually can be described as Mn-doped TiO_2/α-Mn_2O_3.

The UV-visible reflectance spectra of **1** were taken after sintered at different temperatures (Figure 9). However, the presence of low band gap α-Mn_2O_3 masks the optical properties of Mn-doped TiO_2. Assuming a direct band gap for α-Mn_2O_3, the modified Kubelka-Munk function $[F(R)hv]^2$ *vs.* incident photon energy was plotted and the band gap width was estimated to be *ca.* 1.80 eV after 600 °C sintering. Such a band gap agrees well with the literature value for α-Mn_2O_3 (1.2–2.1 eV).[39,40] XPS data suggests a Ti : Mn ratio of (3.57 ± 0.08) : 1 on the surface of the nano-particulate material (Figure S6, ESI) generated after 600 °C sintering, lower than that in the cage molecule (4.5 : 1). This may indicate that, along with the phase separation into α-Mn_2O_3 and TiO_2, the manganese species formed tend to reside at the nanoparticle surface. Such an α-Mn_2O_3/TiO_2 hybrid material could have many applications, and a survey of the literature reveals that MnO_x/TiO_2 has been employed in a range of catalytic and photocatalytic studies.[41-45] However, to our knowledge **1** is the first single-source precursor to this type of material.

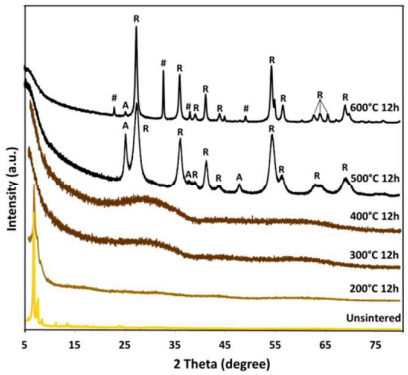

Figure 8. Powder-XRD patterns of the compound **1** and sintered samples at various temperatures. The material converts to TiO_2 at 500 °C. "A" denotes anatase and "R" denotes rutile. The line colours reflect the actual physical appearance of the respective sample. Some extraneous peaks are also present in the "600 °C 12h" spectrum, denoted as "#", which can be well assigned to α-Mn_2O_3.

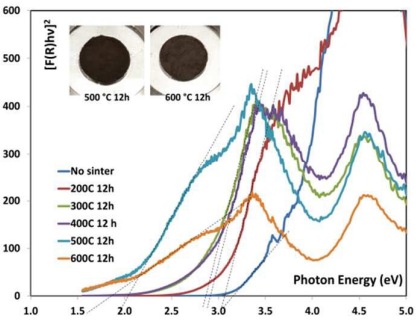

Figure 9. The modified Kubelka-Munk function $[F(R)hv]^2$ for powdered compound **1** (assuming direct allowed band gap model) after sintered at various temperatures. The linear extrapolation to x-axis occurs at 3.15 eV, 3.05 eV, 2.90 eV, 2.85 eV, 2.05 eV and 1.80 eV as the sintering temperature increases. Inset is the digital photograph of the 500 °C and 600 °C sintered samples.

Conclusions

We have synthesized a novel heterometallic polyoxotitanate cage $[Ti_{18}MnO_{30}(OEt)_{20}(MnPhen)_3]$ (**1**) with a unique C_3-core structure. This is the first example of a M-POT cage with the

Dalton Transactions Accepted Manuscript

Please do not adjust margins

same kind of metal dopant ions (Mn^{II}) in two distinct coordination environments. The cage is air/water-stable and even survives the aqueous electrochemical measurements. Optical spectroscopy suggests a direct 'band gap' (HOMO/LUMO) of *ca.* 2.95 eV for **1**. Electrochemical analysis shows two redox couples that probably arise from the two distinct Mn^{II} coordination environments in a single cage molecule. Sintering of **1** at 600°C produces a black material consisting of Mn-doped TiO_2 and α-Mn_2O_3, which exhibits a direct band gap of *ca.* 1.80 eV. To our knowledge **1** is the first single-source precursor to such a composite material of α-Mn_2O_3/TiO_2.

Experimental Section

All chemicals were purchased from commercial sources and used as received, unless otherwise stated. Strict inert-atmospheric conditions (dry and O_2-free) were employed throughout all synthetic and handling procedures [i.e., vacuum-line and using a glove box (Saffron type α)]. IR spectra were obtained using a PerkinElmer Universal ATR spectrometer. Elemental analysis was obtained using a Perkin-Elmer 240 Elemental Analyser. Powder-XRD was performed using PANalytical EMPYREAN Series 2 in a 2θ range of 5-80°. TGA data was acquired on a Mettler Toledo TGA/DSC 2 with gas-phase mass spectrometry. The optical behaviour in the UV-Vis range (200-800 nm) was measured using VARIAN-50 Bio UV-Visible Spectrophotometer. SEM images were taken using a JOEL JSM-5510LV scanning electron microscope. X-ray photoelectron spectra were obtained at the National EPSRC XPS Users' Service (NEXUS) at Newcastle University.

‡ Synthesis of **1**: Titanium ethoxide (2.0 mL, 9.5 mmol), manganese (III) acetate dihydrate (140 mg, 0.5 mmol), 1,10-phenanthroline (90 mg, 0.5 mmol) and anhydrous ethanol (10.0 mL, 170 mmol) were loaded into a teflon-lined autoclave and heated at 150 °C for 72 hours. Gradually cooling down to room temperature produced block-shape orange coloured crystals of **1**. The crystals were filtered off at room temperature and washed with anhydrous ethanol before being dried *in vacuo* (80 mg, 20% yield with respect to $Mn(AcO)_3{\cdot}(H_2O)_2$ supplied). Replacing $Mn(AcO)_3{\cdot}(H_2O)_2$ by $Mn(AcO)_2{\cdot}(H_2O)_4$ produced the sample species but in a lower yield. IR (solid powder) ν/cm^{-1}: 2967 (m), 2920 (m), 2859 (m) (C-H str. EtO), 3090 (w) (C-H aryl, 1,10-phenanthroline), 1429 (m), 1373 (m), 1131 (s), 1099 (s), 1067 (s), 1040 (s), 919 (m), 892 (m), 842 (s) and 715 (s). Elemental analysis (%), cald. for compound **1** C 30.4, H 4.2, N 2.8, found (average of four measurements) C 31.1, H 4.3, N 2.7. M.pt. decomp. 300-350 °C.

§ *X-ray Crystallography on* **1**: Crystallographic data were collected on a Nonius Kappa CCD diffractometer using Mo(K_α) radiation (λ = 0.71073 Å). The structure was solved and refined by full matrix least-squares on F^2 using the SHELX programme.[46] All non-hydrogen atoms were refined anisotropically. The hydrogen atoms were introduced in to calculated positions and refined with fixed geometry with respect to their C atoms. The data and refinement are summarized and shown in Table 1. CCDC number 1423275 contains the crystallographic files for **1**.

Table 1 Crystal data and structure refinement for compound **1**

Empirical Formula	$C_{76}H_{124}Mn_4N_6O_{50}Ti_{18}$
Formula Weight	3003.76
Temperature	180(2) K
Wavelength	0.71073 Å
Crystal System	Monoclinic
Space group	$P2_1/c$
Unit cell dimension	a = 15.723(3) Å α = 90° b = 23.832(5) Å β = 96.44(3)° c = 31.971(6) Å γ = 90°
Volume	11905(4) $Å^3$
Z	4
Density (calculated)	1.676 Mg/m^3
Absorption coefficient	1.621 mm^{-1}
F(000)	6072
Crystal size	0.460 × 0.460 × 0.460 mm
Theta range for data collection	3.516 to 25.054
Index range	-18≤ h ≤18, -27≤ k ≤28, -35≤ l ≤38
Reflections collected	61565
Independent reflections	19760 [R(int) = 0.052]
Completeness to theta = 22.211	93.8%
Absorption correction	Semi-empirical from equivalents
Max. and min. transmission	0.492 and 0.420
Refinement method	Full-matrix least-squares on F^2
Data / restraints / parameters	19760 / 582 / 1317
Goodness-of-fit on F2	1.025
Final R indices [I>2sigma(I)]	R1 = 0.099, wR2 = 0.271
R indices (all data)	R1 = 0.152, wR2 = 0.314
Largest diff. peak and hole	1.414 and -0.824 $e.A^{-3}$

§§ *Solid State Electrochemistry on* **1**: The electrodes for electrochemical measurement were made by drop-casting fresh solutions of **1** onto clean FTO-coated glass (exposed area of 1.0 cm^2). The solution was prepared by dissolving 10 mg of **1** in 4.0 mL of a toluene/methanol mixture (3:2 in volume). 90 uL of this solution was drop-cast onto FTO using a pipette at 80 °C in air and dried in the same condition. The as-prepared electrode was then immersed into an electrochemical cell containing an aqueous solution of sodium sulphate (Na_2SO_4, 0.1 M, pH 6.54) electrolyte. The electrochemical experiments were performed using a conventional three-electrode system with the as-prepared working electrode, a Pt foil counter electrode and an Ag/AgCl/saturated KCl reference electrode at room temperature. The electrolyte was purged with N_2 for 1 hour before use.

§§§ *Solution Phase Electrochemistry on* **1**: The solution phase CV was conducted using glassy carbon as working, Pt mesh as counter and Ag/AgCl Tol/MeOH as reference electrodes in a saturated solution of compound **1**. The solution was prepared by adding 90 mg of crystal **1** in 3 mL of toluene and methanol mixture (3:2 volume ratio). After 30 min stirring at room temperature, the yellow cloudy suspension was centrifuged to obtain a clear yellow solution of **1**. 0.1 M NBu_4BF_4 was used as electrolyte and the solution was purged with N_2 for 15 min before measurement.

Dalton Transactions Accepted Manuscript

This journal is © The Royal Society of Chemistry 20xx

Acknowledgements

We thank the AGSO (N.L.), EPSRC (P.D.M., T.C.K.), Woolf Fisher Trust (J.J.L.) and the ERC (Advanced Investigator Grant, D.S.W.) for financial support. Special thanks go to Mr. Paul Skelton for the mass spectrometry study and to Dr. Erwin Reisner and Ms. Yi-Hsuan Lai for their constructive help on electrochemistry. In addition, we are also grateful to National EPSRC XPS Users' Service (NEXUS) at Newcastle University for XPS studies.

Notes and references

1 X. Chen and S. S. Mao, *Chem. Rev.,* 2007, **107**, 2891.
2 U. I. Gaya and A. H. Abdullah, *J. Photochem. Photobiol. C: Photochem. Rev.*, 2008, **9**, 1.
3 M. Pelaez, N. T. Nolan, S. C. Pillai, M. K. Seery, P. Falaras, A. G. Kontos, P. S. M. Dunlop, J. W. J. Hamilton, J. A. Byrne, K. O'Shea, M. H. Entezari and D. D. Dionysiou, *Appl. Catal. B: Environmental*, 2012, **125**, 331.
4 J. B. Benedict, R. Freindorf, E. Trzop, J. Cogswell and P. Coppens, *J. Am. Chem. Soc.*, 2010, **132**, 13669.
5 L. Wu, J. C. Yu, L. Zhang, X. Wang, and W. Ho, *J. Solid State Chem.*, 2004, **177**, 2584.
6 Y.-Y. Wu, P. Wang, Y.-H. Wang, J.-B. Jiang, G.-Q. Bian, Q.-Y. Zhu, J. Dai, *J. Mater. Chem. A*, 2013, **1**, 9862.
7 J.-X. Yin, P. Huo, S. Wang, J. Wu, Q.-Y. Zhu and J. Dai, *J. Mater. Chem. C*, 2015, **3**, 409.
8 Y.-Y. Wu, X.-W. Lu, M. Qi, H.-C. Su, X.-W. Zhao, Q.-Y. Zhu and J. Dai, *Inorg. Chem.*, 2014, **53**, 7233.
9 S. Wang, H.-C. Su, L. Yu, X.-W. Zhao, L.-W. Qian, Q.-Y. Zhu and J. Dai, *Dalton Trans.*, 2015, **44**, 1882.
10 K. N. Jarzembska, Y. Chen, J. N. Nasca, E. T. Trzop, D. F. Watson and P. Coppens, *Phys. Chem. Chem. Phys.*, 2014, **16**, 15792.
11 Y.-Y. Wu, W. Luo, Y,-H. Wang, Y.-Y. Pu, X. Zhang, L.-S. You, Q.-Y. Zhu and J. Dai, *Inorg. Chem.*, 2012, **51**, 8982.
12 R. C. Snoeberger, K. J. Young, J. Tang, L. J. Allen, R. H. Crabtree, G. W. Brudvig, P. Coppens, V. S. Batista and J. B. Benedict, *J. Am. Chem. Soc.*, 2012, **134**, 8911.
13 J. D. Sokolow, E. Trzop, Y. Chen, J. Tang, L. J. Allen, R. H. Carbtree, J. B. Benedict and P. Coppens, *J. Am. Chem. Soc.*, 2012, **134**, 11695.
14 J. B. Benedict and P. Coppens, *J. Am. Chem. Soc.*, 2010, **132**, 2938.
15 Y. Chen, E. Trzop, A. Makal, J. D. Sokolow and P. Coppens, *Inorg. Chem.*, 2013, **52**, 4750.
16 S. Eslava, B. P. R. Goodwill, M. McPartlin and D. S. Wright, *Inorg. Chem.*, 2011, **50**, 5655.
17 Y. Lv, J. Cheng, P. D. Matthews, J. P. Holgado, J. Willkomm, M. Leskes, A. Steiner, D. Fenske, T. C. King, P. T. Wood, L. Gan, R. M. Lambert and D. S. Wright, *Dalton Trans.*, 2014, **43**, 8679.
18 S. Eslava, M. McPartlin, R. I. Thomson, J. M. Rawson and D. S. Wright, *Inorg. Chem.*, 2010, **49**, 11532.
19 Y. Chen, E. Trzop, A. Makal, Y.-S. Chen and P. Coppens, *Dalton Trans.*, 2014, **43**, 3839.
20 Y. Chen, J. Sokolow, E. Trzop, Y.-S. Chen and P. Coppens, *J. Chin, Chem. Soc.*, 2013, **60**, 887.
21 Y. Lv, J. Cheng, A. Steiner, L. Gan and D. S. Wright, *Angew. Chem. Int. Ed.*, 2014, **53**, 1934.
22 S. Eslava, F. Hengesbach, M. McPartlin and D. S. Wright, *Chem. Commun.*, 2010, **46**, 4701.
23 Y.-H. Lai, C.-Y. Lin, Y. Lv, T. C. King, A. Steiner, N. M. Muresan, L. Gan, D. S. Wright and E. Reisner, *Chem. Commun.*, 2013, **49**, 4331.
24 Y. Lv, J. Willkomm, A. Steiner, L. Gan, E. Reisner and D. S. Wright, *Chem. Sci.*, 2012, **3**, 2470.
25 Y.-H. Lai, T. C. King, D. S. Wright and E. Reisner, *Chem. Eur. J.*, 2013, **19**, 12943.
26 Y. Lv, J. Willkomm, M. Leskes, A. Steiner, T. C. King, L. Gan, E. Reisner, P. T. Wood and D. S. Wright, *Chem. Eur. J.*, 2012, **18**, 11867.
27 Y. Lv, M. Yao, J. P. Holgado, T. Roth, A. Steiner, L. Gan, R. M. Lambert and D. S. Wright, *RSC Adv.*, 2013, **3**, 13659.
28 P. D. Matthews, T. C. King and D. S. Wright, *Chem. Commun.*, 2014, **50**, 12815.
29 L. Rozes and C. Sanchez, *Chem. Soc. Rev.*, 2011, **40**, 1006.
30 P. Coppens, Y. Chen and E. Trzop, *Chem. Rev.*, 2014, **114**, 9645.
31 B. Liu, H. M. Chen, C. Liu, S. C. Andrews, C. Hahn and P. Yang, *J. Am. Chem. Soc.*, 2013, **135**, 9995.
32 R. Daghrir, P. Drogui and D. Robert, *Ind. Eng. Chem. Res.*, 2013, **52**, 3581.
33 K. Gigant, A. Rammal and M. Henry, *J. Am. Chem. Soc.*, 2001, **123**, 11632.
34 M. G. Davidson, M. D. Jones, M. D. Lunn and M. F. Mahon; *Inorg. Chem.*, 2006, **45**, 2282.
35 Y. Gorlin and T. F. Jaramillo, *J. Am. Chem. Soc.*, 2010, **132**, 13612.
36 C. Bosch-Navarro, E. Coronado, C. Martí-Gastaldo, B. Rodríguez-González and L. M. Liz-Marzán, *Adv. Funct. Mater.*, 2012, **22**, 979.
37 R. Schmid. A. Mosset and J. Galy, *J. Chem. Soc. Dalton Trans.*, 1991, 1999.
38 L. Lu, X. Xia, J. K. Luo and G. Shao, *J. Phys. D: Appl. Phys.*, 2012, **45**, 485102.
39 Q. Javed, F. P. Wang, M. Y. Rafique, A. M. Toufiq, Q. S. Li, H. Mahmood and W. Khan, *Nanotechnology*, 2012, **23**, 415603.
40 Q. Javed. F. P. Wang, M. Y. Rafique, A. M. Roufiq and M. Z. Iqbal, *Chin. Phys. B*, 2012, **21**, 117311.
41 Q. Jin, H. Arimoto, M. Fujishima and H. Tada, *Catalysts*, 2013, **3**, 444.
42 A. Aboukaïs. E. Abi-Aad and B. Taouk, *Mater. Chem. Phys.*, 2013, **142**, 564.
43 N. Li, W.-Y. Xia, J. Wang, Z.-L. Liu, Q.-Y. Li, S.-Z. Chen, C.-W. Xu and X.-H. Lu, *J. Mater. Chem. A*, 2015. DOI: 10.1039/C5TA04964D
44 X. Lu, C. Song, C.-C. Chang, Y. Teng, Z. Tong and X. Tang, *Ind. Eng. Chem. Res.*, 2014, **53**, 11601.
45 P. R. Ettireddy, N. Ettireddy, S. Mamedov, P. Boolchand and P. G. Smirniotis, *Appl. Catal. B: Environmental*, 2007, **76**, 123.
46 G. M. Sheldrick, *Acta. Crystallogr.*, 2008, **64**, 112.

Dalton Transactions Accepted Manuscript

Journal Name

ARTICLE

The novel Mn-doped polyoxotitanate $[Ti_{18}MnO_{30}(OEt)_{20}(MnPhen)_3]$ has a unique arrangement for a polyoxotitanium cage and is shown to decompose thermally into α-Mn_2O_3/TiO_2.

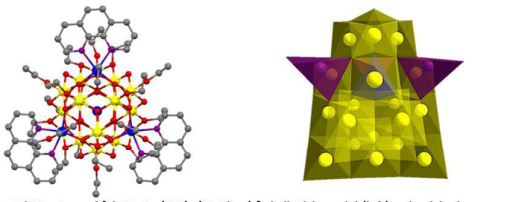

Crystal Structure of $[Ti_{18}MnO_{30}(OEt)_{20}(MnPhen)_3]$: ball-stick model (left) and polyhedron representation of the core (right).

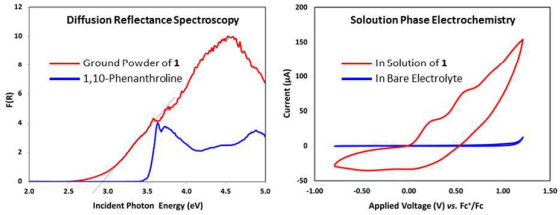

Dalton Transactions Accepted Manuscript